MATERIALS SCIENCE

A CMOS-based highly scalable flexible neural electrode interface

Eric T. Zhao[1], Jacob M. Hull[2], Nofar Mintz Hemed[3], Hasan Uluşan[4], Julian Bartram[4], Anqi Zhang[1], Pingyu Wang[3], Albert Pham[3], Silvia Ronchi[4], John R. Huguenard[2], Andreas Hierlemann[4], Nicholas A. Melosh[3]*

Perception, thoughts, and actions are encoded by the coordinated activity of large neuronal populations spread over large areas. However, existing electrophysiological devices are limited by their scalability in capturing this cortex-wide activity. Here, we developed an electrode connector based on an ultra-conformable thin-film electrode array that self-assembles onto silicon microelectrode arrays enabling multithousand channel counts at a millimeter scale. The interconnects are formed using microfabricated electrode pads suspended by thin support arms, termed Flex2Chip. Capillary-assisted assembly drives the pads to deform toward the chip surface, and van der Waals forces maintain this deformation, establishing Ohmic contact. Flex2Chip arrays successfully measured extracellular action potentials ex vivo and resolved micrometer scale seizure propagation trajectories in epileptic mice. We find that seizure dynamics in absence epilepsy in the *Scn8a*$^{+/-}$ model do not have constant propagation trajectories.

INTRODUCTION

Perception, thoughts, and actions involve the coordinated activity of large populations of neurons in multiple regions of the brain (*1*–*3*). Nonpenetrative, subdural ECoG grids laid on top of the brain surface are the gold standard for recording population-level activity, measured from the local field potential (LFP). Neurophysiological recordings with ECoG grids have been successfully used for speech synthesis (*4*, *5*), reproduction of arm movements (*6*), and spatial localization of ictal onset zones (*7*). They have also been used to characterize cortical traveling waves (*8*), which have been shown to modulate perceptual sensitivity (*9*). Hence, ECoG grids are a favorable modality for brain-computer interface applications, localization of epileptic foci for clinical epilepsy diagnosis and targeted tissue resection, and as a basic science tool.

Ultraconformable thin-film flexible devices that can conform to the curvilinear surface of the brain are a promising technology to capture cortex-wide spatiotemporal dynamics (*10*–*12*). Microfabrication and advanced lithography methods have enabled the creation of thin-film arrays with hundreds to thousands of recording sites (*13*, *14*). However, the key bottleneck lies not in the fabrication of these devices but in the connectorization between each electrode and the external circuitry. Because of the bulkiness of existing connectorization methods such as wire bonding, anisotropic conductive film (*15*), and ultrasonic-on-bump bonding (*16*), current implementations of multithousand channel count, passive thin-film neural interfaces are highly complex, bulky, and unscalable. Examples include the stacking of 16 application-specific integrated circuits (ASICs) on eight circuit boards to achieve 1024 channels (*17*, *18*), modularization of 12 ASICs on a single circuit board for 3072 channels (*19*), and the use of 2 central processing unit sockets, 2 circuit boards, and 32 ASICs for 2048 channels (*11*).

Consequently, the field has focused on adapting this technology for active, multiplexed thin-film arrays that monolithically integrate the recording electrodes with amplifiers and analog-to-digital converters, bypassing the one electrode per input/output (I/O) limit (*12*, *20*). However, these active thin-film arrays suffer from increased noise, subkilohertz sampling rates, lower channel counts, and substantially increased device size due to the difficulty in fabricating high-mobility, high mechanical flexibility, and small-size flexible transistors (*21*). On the other hand, silicon-based large-scale complementary metal-oxide semiconductor microelectrode arrays (CMOS-MEAs) have built on decades of development in active pixel sensors, traditionally used in cameras, to provide excellent signal-to-noise ratio, high sampling rates, and scalability up to tens of thousands of channels at high densities (*22*–*24*). However, their rigid form factor is incompatible for interfacing with the brain surface.

Here, we sought to combine the scalability and exceptional performance of CMOS-MEAs with the ultraconformable form factor of flexible devices. We achieve this by developing a scalable, high-density connectorization strategy, which can form thousands of interconnections between the electrode pads on the flexible device and the pixels on the CMOS-MEA at a high density. The flexible device extends out from the CMOS-MEA through long leads, converging at the distal end as an array that interfaces with the brain (Fig. 1A).

We design a microstructure, termed Flex2Chip, which consists of microfabricated 1-μm-thick and 2-μm-wide supporting arms suspending each individual electrode pad. We leverage the ultra-compliant nature of the supporting arms to allow capillary and van der Waals forces to deform the pad to establish mechanical and electrical contact with the underlying pixels (Fig. 1B). This Flex2Chip interconnection is self-assembled and does not require any equipment or lithographic postprocessing to facilitate electrical connectivity. After assembly, the device could be encapsulated with silicone at high yield to provide mechanical robustness. We demonstrate a 2200-channel device with a connection interface area of 3.85

[1]Department of Chemical Engineering, Stanford University, Stanford, CA, USA. [2]Department of Neurology, Stanford University, Stanford, CA, USA. [3]Department of Materials Science and Engineering, Stanford University, Stanford, CA, USA. [4]Department of Biosystems Engineering, ETH Zürich, Basel, Switzerland.
*Corresponding author. Email: nmelosh@stanford.edu

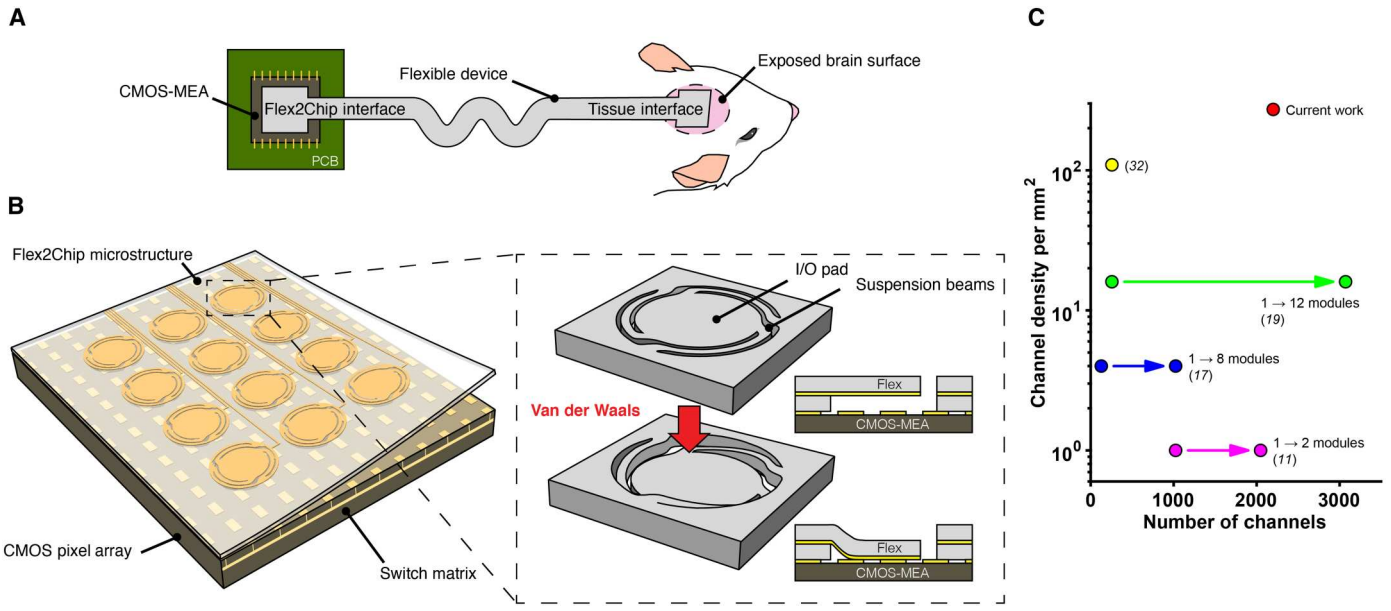

Fig. 1. Flex2Chip design. (**A**) Schematic of the flexible device. At the chip interface, Flex2Chip microstructures enable multithousand ohmic interconnections to a CMOS-MEA. At the tissue interface, the device terminates as an electrode array for high density recording. (**B**) Flex2Chip interface consists of an array of deformable Flex2Chip microstructures, integrated with the underlying CMOS-MEA. The Flex2Chip microstructures consist of three suspended beams and an I/O pad. Capillary forces deform the I/O pad to contact the CMOS pixels, upon which van der Waals forces become significant to establish structural and electrical contact. (**C**) Current approaches to multithousand channel counts rely on the modularization of multiple ASICs and circuit boards. The Flex2Chip structures facilitate 2200 individual ohmic connections to a single ASIC with an area of 3.5 mm by 2.1 mm, yielding a channel density of 272 channels/mm^2.

mm by 2.1 mm, 17 times denser than that of current multithousand-channel devices (Fig. 1C). Our method could achieve multithousand-channel counts without relying on the modularization of multiple ASICs and circuit boards.

We further show the utility of our devices in neuroscience and biologically relevant applications. We validate that our device can record extracellular action potentials with a high signal-to-noise ratio in acute ex vivo cerebellar slices. Last, we demonstrate the efficacy of our device and its potential clinical utility through the detection and characterization of submillimeter traveling waves during absence seizures on the cortical surface of awake and behaving epileptic mice. Here, our high-density flexible probes combined with the temporal resolution of the CMOS-MEA enabled the observation of highly variable propagation trajectories at micrometer scales even across the duration of a single spike-and-wave discharge (SWD).

RESULTS

System design and connectorization for the Flex2Chip devices and microstructures

The Flex2Chip devices were fabricated using standard microfabrication procedures (Materials and Methods). The devices consist of a 2200-channel array of 1-μm-wide and 100-nm-thick platinum leads at a 2-μm pitch, sandwiched between two 1-μm-thick polyimide sheets that serve as substrate and dielectric layers (Fig. 1A). At the Flex2Chip interface, these leads branch out to an array of I/O pads, which interface with the CMOS-MEA (Fig. 1B and fig. S1A). At the tissue interface, the leads branch out into an array of recording/stimulation pads (fig. S1, B and C).

At the Flex2Chip interface, the dielectric layer is etched so that the conductive I/O pad is exposed. However, the pad is recessed by 1 μm and unable to directly contact external circuitry. Unlike previous approaches, which rely on the addition of external components, e.g., gold wires for wire bonding and microparticles for anisotropic conductive films, we instead modified the I/O pad itself to facilitate connectorization.

Here, we developed a microstructure on the I/O pad, termed Flex2Chip, enabling the pad to deform downward to mate with contact pads on external circuitry. The Flex2Chip consists of a 35-μm-diameter I/O pad suspended by three suspension beams, 2-μm wide and 10-μm long (Fig. 1B, inset top, and fig. S2). The conductive leads run from the I/O pad, across the suspension beams, and onto the main substrate.

The low-bending stiffness and flexibility of the suspension beams permit the I/O pad to deform relative to the flexible device and toward the underlying pixel on the CMOS array under capillary forces (see the section below) until the platinum electrodes make physical and electrical contact with the gold-plated pixels, upon which van der Waals forces hold the microstructure in its collapsed configuration (Fig. 1B, inset bottom).

We included three suspension beams that mechanically prevent the pad from twisting or flipping over during handling and assembly. The interelectrode pitch was set at 50 μm (Fig. 2, A and B, and fig. S2D), greater than the pixel pitch, so that adjacent pads will not be shorted (*22*, *25*, *26*). This simplifies assembly, allowing rotational and translational degrees of freedom.

At the tissue interface, the leads fan out to an array of recording/stimulation pads (fig. S1C). The distal end geometry can be freely customized for the specific biological system of interest. For

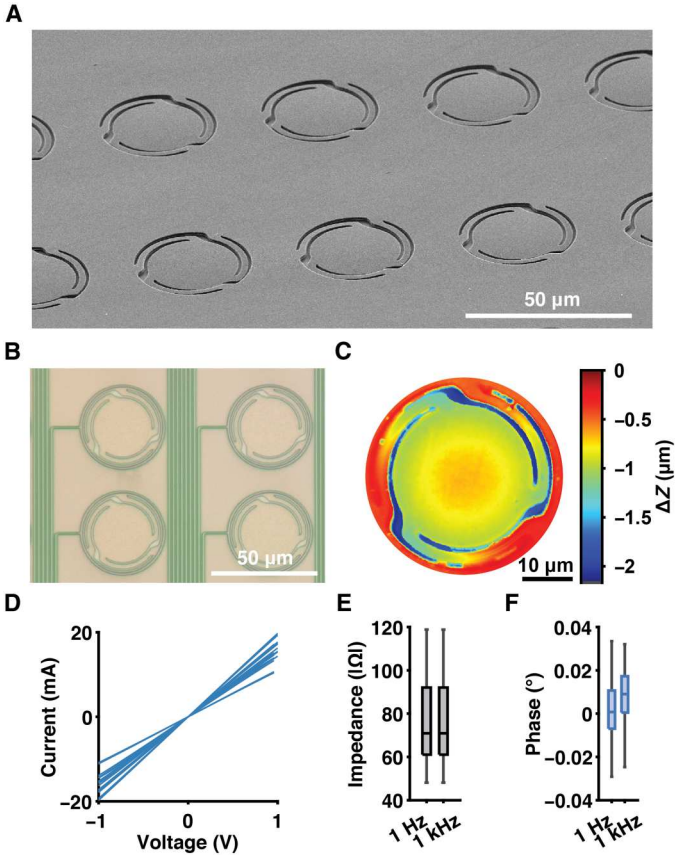

Fig. 2. Flex2Chip structure and electrical characteristics. (**A**) SEM image of the Flex2Chip device laid on top of a planar glass surface. A slight deformation of the 40-µm-diameter I/O pad toward the underlying surface enabled by the suspension beams can be observed. (**B**) Each Flex2Chip microstructure is routed by a 1-µm-wide trace toward the distal end of the device, terminated by a recording/stimulation pad. (**C**) Optical profilometer measurement confirms that the Flex2Chip I/O pad has fully deformed by 1 µm to contact the underlying surface and that van der Waals forces are sufficient to hold the structure in its deformed configuration, which facilitates stable mechanical contact. (**D**) Contact is ohmic, as seen in the resistive behavior of the *I-V* curve (n = 18). (**E**) Impedance magnitude of the Flex2Chip interface is 76.7 ± 20.0 and 76.7 ± 20 ohm at 1 and 1000 Hz, respectively (n = 64). (**F**) Phase of the Flex2Chip interface is 0.00° ± 0.01° and 0.01° ± 0.01° at 1 and 1000 Hz, respectively (n = 64).

example, we can have a contiguous sheet for ECoG grids or shanks for intracortical insertion (*18*).

Microstructure deformation assisted by capillary assembly

We leverage the flexibility of the Flex2Chip microstructures to establish connectorization between the I/O pad and CMOS-MEA pixel. This deformation is achieved under the action of capillary and van der Waals forces, which operate at micrometer- and nanometer-length scales, respectively. When the flexible device is placed on the CMOS-MEA, the I/O pad is 1 µm away from the underlying pixel (the thickness of the dielectric layer) (Fig. 1B, inset top). We initiate the microstructure deformation by applying a thin layer of isopropyl alcohol (IPA) between the device and CMOS-MEA. The capillary force of the liquid bridge formed between the I/O pad, and the pixel "pulls" the pad toward the pixel as the solvent evaporates. After the IPA fully evaporates and the pad reaches its fully collapsed structure, van der Waals forces become significant enough to hold the microstructure in its collapsed configuration (Fig. 1B, inset bottom).

We characterized this deflection by assembling a device on a CMOS-MEA phantom. Optical profilometry of the Flex2Chip microstructures showed that the structures have fully deformed and contacted the underlying chip (Fig. 2C). The deformation was observed to be uniformly distributed across the three suspension beams, and the I/O pad was uniformly displaced by 1 µm relative to the bulk device. The center of the I/O pad was slightly curved upward, indicative of residual stress from the device fabrication. Scanning electron microscopy (SEM) images also support the optical profilometer results, with a slight deformation visible despite its 1:40 aspect ratio (Fig. 2A).

The electrical characteristics of the Flex2Chip microstructure interface were evaluated to assess the quality of electrical contact and whether stray capacitance was introduced, which may affect the quality of the recording, electrical stimulation, or electrochemical measurements. Here, we shorted the distal end of the Flex2Chip device to a gallium droplet as a liquid contact. The current-voltage characteristic curve [current-voltage relation (*I-V*)] exhibits a clear linear relationship, characteristic of Ohmic resistors, with a resistance of 66.5 ± 12.9 ohm (Fig. 2D and fig. S3A). Furthermore, impedance spectroscopy indicated an ohmic connection between the microstructure and chip, with an average phase of 0.00° ± 0.01° and 0.01° ± 0.01° at 10 and 1000 Hz, respectively (Fig. 2, E and F, and fig. S3B). This finding confirmed that there is no capacitive impedance at the physiological frequencies of interest. Impedance contributions included cumulative contributions from the Flex2Chip interface and trace resistances but were insignificant compared to electrode-electrolyte impedance.

Electrical performance through CMOS-MEA

Having confirmed the quality of the mechanical and electrical contact of our Flex2Chip structures, we sought to characterize the electrode yield and recording quality of our device using a CMOS-MEA recording chip. Here, we fabricated a 720- and 2200-channel Flex2Chip array (figs. S1A and S5A). The I/O pads are distributed across a 3.85 mm–by–2.10 mm area, the active dimensions of the CMOS-MEA (MaxWell Biosystems Inc., Zurich, Switzerland), which has 26,400 active pixel sensors at a pitch of 17.5 µm. As our interelectrode pitch is greater than the pixel pitch, no alignment is needed during assembly.

We evaluated the connectivity yield of the device by applying a sinusoidal waveform across all the electrodes. We submerged the distal end of the device (figs. S1, B and C, and S5, B and C) in a phosphate-buffered saline (PBS) bath along with a Pt reference electrode. We applied a sinusoidal waveform at 1 kHz at the reference electrode and scanned the response of each of the 26,400 active pixel sensors. The pixels that were connected to our Flex2Chip microstructure subsequently then recorded the resulting waveform (Fig. 3A). By cross-referencing with the geometry of the flexible array (Fig. 3B), the position of each microstructure on the CMOS-MEA was localized. As the CMOS-MEA can only measure from 1024 channels simultaneously, we programmed the switch matrix to select only the pixels that corresponded to the individual microstructures to record from.

We then deposited platinum black (Pt black) on the electrode pads to reduce the signal attenuation, Johnson-Nyquist noise, and

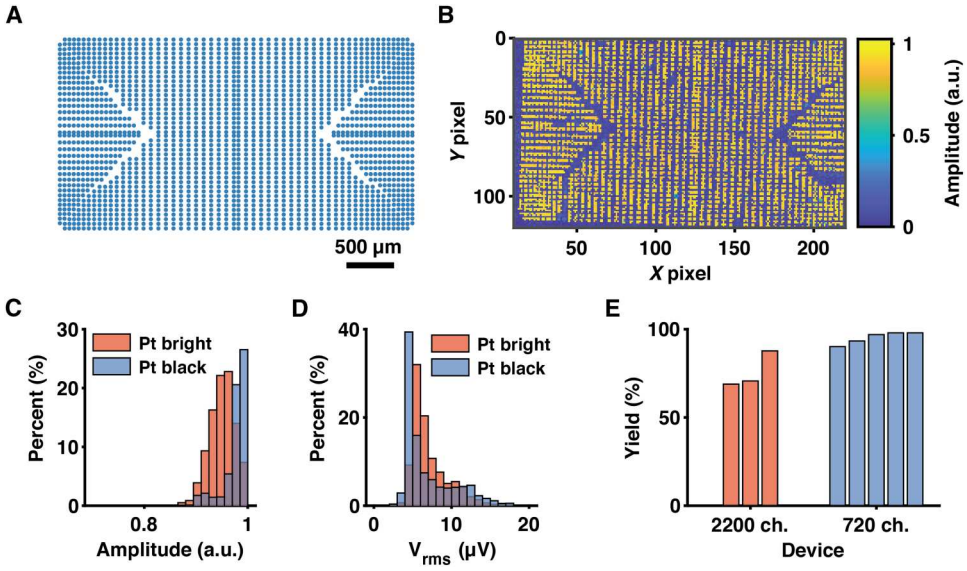

Fig. 3. Connectivity to the CMOS-MEA. (**A**) Flex2Chip pad layout. The traces are routed out on all four sides to maximize the pad density interfacing with the CMOS-MEA, as seen in fig. S5A. (**B**) Heatmap of the relative signal amplitude measured by each pixel in the CMOS-MEA. The signal is generated through the reference electrode in a saline bath by an external function generator. (**C**) Histogram of the relative signal amplitude of the pixels connected to the Flex2Chip microstructures. Bright platinum electrodes detected 0.95 ± 0.03, and platinum black–coated electrodes detected 0.99 ± 0.03 with respect to the full-scale injected signal, indicative of minimal attenuation. (**D**) Histogram of the RMS noise was 7.13 ± 2.33 μV for bright platinum and 6.93 ± 3.31 μV for platinum black electrodes. (**E**) Average connectivity yield of the 2200-channel device and 720-channel device was 75.7 and 95.3%, respectively. a.u., arbitrary units.

interelectrode cross-talk (*27*). Here, we leveraged the stimulation units of the CMOS-MEA for voltage-controlled electrochemical deposition at −0.5 V at the working electrode for 40 s. With bare platinum (Pt bright), the pixels detected 0.95 ± 0.03 of the injected sine wave signal, a 5% attenuation. This was further reduced by Pt black, which detected 0.99 ± 0.03 with respect to the full-scale injected signal (Fig. 3C). The root mean square (RMS) noise was also low, with platinum bright 7.13 ± 2.33 μV and platinum black 6.93 ± 3.31 μV, minimally higher than that of the bare pixels 5.00 ± 1.50 μV (*25*).

The developed connectorization methodology is also highly reliable with an average connectivity yield of 95.3 ± 3.42 and 75.7 ± 10.4% for a 720-channel and a 2200-channel device, respectively (Fig. 3E). The ultralow footprint of the device is highlighted with a 720-channel device for in vivo recordings as shown in fig. S2C. We also assessed the stability of the interconnection in an incubator over a month (37°C, 97% humidity, Heracell 150i, Thermo Fisher Scientific Inc., MA, USA). The yield is virtually unchanged, decreasing from 709 to 705 of 720 channels (fig. S3D), with no decrease in the sensitivity (0.99 ± 0.03) (fig. S3E).

Encapsulation

Although ohmic connectivity was established, the connection interface is only held with van der Waals forces and is delicate to external mechanical forces. The interface can be secured by applying a liquid silicone elastomer (KwikSil), which upon curing, seals the pads in place and provides a mechanically robust encapsulation layer. This encapsulation method minimally affects the channel yield, with a decrease of 9.38 ± 14.6% (fig. S4A).

The encapsulated interface was robust and could withstand a tensile force of 268 ± 6.65 mN before breakage and loss of electrical connectivity (fig. S4B). The failure occurred along the interconnect lead rather than the device itself. This is more than sufficient for a head-mounted device as in a chronic animal setup, slack in the lead cable would be introduced to mitigate any tensile forces that the device will experience between the brain and skull. Last, the electrical performance was not affected, with no statistically significant differences in the impedance or phase after encapsulation (fig. S4, C to F).

Multisite brain slice electrophysiology

Having prepared our Flex2Chip device, we then tested its ability to record neural activity in an ex vivo preparation of an acute cerebellar brain slice. Here, we used a 720-channel device, where the recording end covers an area of 3.6 mm by 1.62 mm with 90-μm pitch (30 × 24 array) with 20-μm-diameter electrode pads (fig. S5, C and D). The dimensions and channel count of the device were chosen to match the size of the tissue slice. The 720-channel device was attached to a 6-mm-diameter stainless steel ring, and the weighted construct was placed on top of the slice (fig. S6). The device was fenestrated with 60 μm–by–80 μm holes between each electrode to allow sufficient nutrient and oxygen diffusion to keep the slice healthy for the duration of the experiment. As seen in the bright-field microscopy image in Fig. 4A, the neurons were on the same focal plane as the device, indicating good contact.

We observed spontaneous spiking activity and isolated 36 individual units from various spatial locations of the slice (Fig. 4, B and C). Units were well isolated as indicated by interspike interval (ISI) violations within the refractory period (±1.5 ms) below 0.1. The clearly defined peaks in the autocorrelograms demonstrate regular firing behavior typical of cerebellar Purkinje cells (*28*). With an electrode pitch of 90 μm, we successfully detected the same neuron across multiple electrodes so that we were able to establish a neural footprint, that is, the spike-triggered average electrical

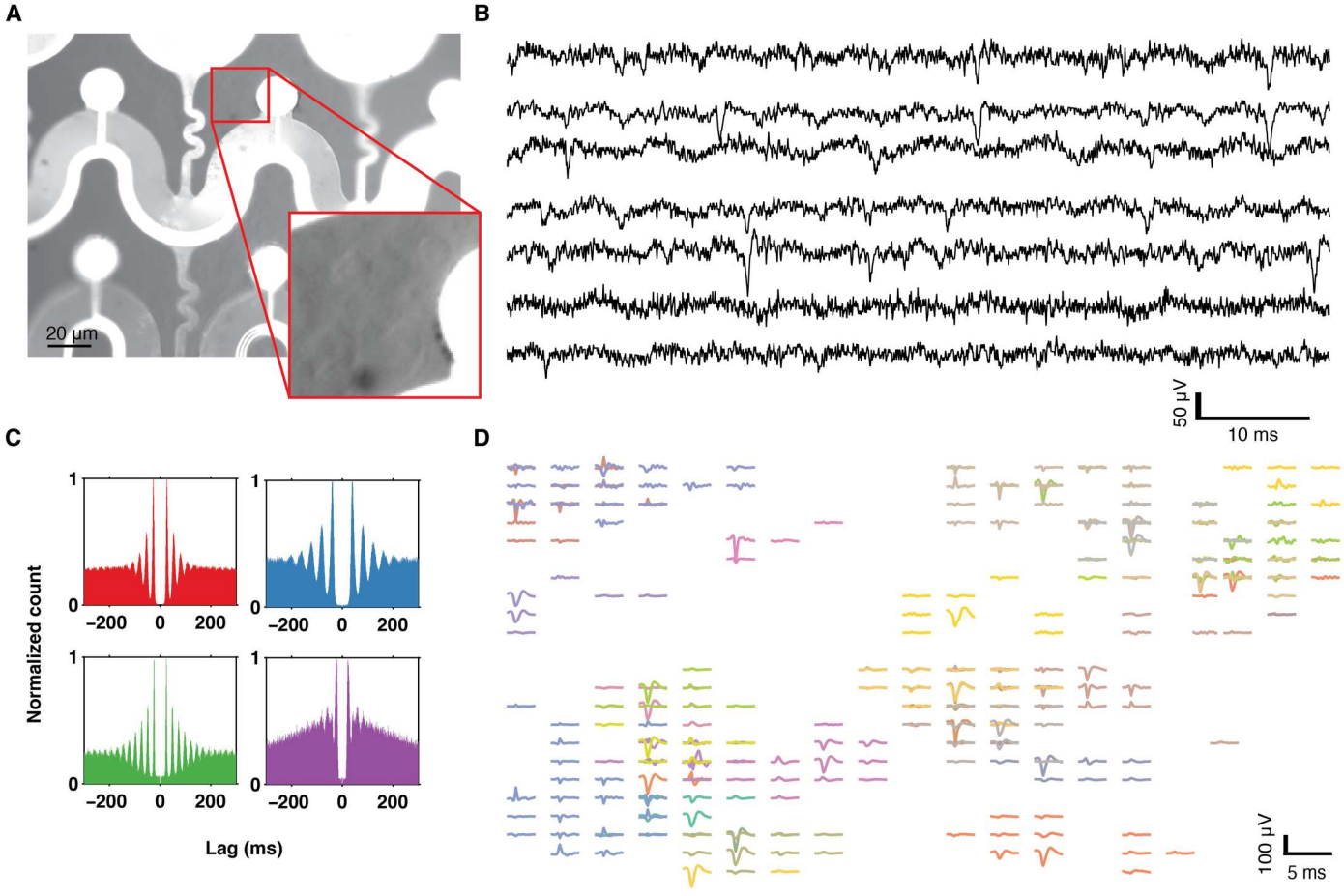

Fig. 4. In vitro cerebellar slice recordings. (**A**) Microscopy of the fenestrated 720-channel device. The device and the cerebellar cells were in the same focal plane. The inset has adjusted brightness and contrast highlighting the cerebellar cells. (**B**) Representative traces off the 720-channel device with a 50-Hz notch filter. (**C**) Spike autocorrelograms of cerebellar cells exhibiting regular firing behavior, spanning ±300 ms and a bin size of 5 ms. The peaks show that the spiking activity occurred at a regular period characteristic of Purkinje cells. (**D**) Spike-triggered average waveform of individually sorted units plotted spatially across the electrodes.

potential distribution across electrodes for a specific unit (Fig. 4D). For multiple neurons, we detected both negative and positive amplitude spikes, indicative of the signal originating from the axon initial segment (negative), and dendritic branches (positive) (*29*). This system thus provides a simple, small form-factor method of recording from hundreds to thousands of electrode sites while retaining high-quality recordings and single-spike level sensitivity.

Seizure recordings in awake and behaving mice

We next evaluated the performance of the device in a real-world application as an ECoG grid to track the dynamics of seizure propagation with micrometer precision by placing it on the cortical surface of an epileptic mouse (Fig. 5A). Here, we fabricated a 504-channel device with an active area of 760 μm by 760 μm with 20-μm-diameter electrode pads (Fig. 5B and fig. S5B), customized to record from a 2-mm-diameter craniotomy window above the sensorimotor cortex. The total channel count in this case was constrained simply by the size of the craniotomy. To differentiate local activity at each recording site from volume conducted signals, we used the analytic signal method, which can identify localized instantaneous frequency and phase information (Fig. 5C). The recordings were performed acutely within 2 hours of the device placement onto the exposed motor and somatosensory cortex. Mice were allowed to run voluntarily on a cylindrical treadmill in a head-strained condition while recording with the device and CMOS-MEA.

The transgenic mouse model *Scn8a*$^{+/-}$ exhibits spontaneous absence epilepsy, characterized by brief periods of unconsciousness and lapse in motor function that have a distinct 7-Hz SWD (*30*). Our single-channel measurements showed the stereotypical 7-Hz SWD with a shift toward low-frequency band power across the duration of a single seizure (Fig. 5D).

We computed the instantaneous phase of the LFP signal to characterize the spatiotemporal propagating wave dynamics that occurs during seizures (*31*). Here, we used the generalized phase (GP), an updated approach of the analytic signal to enable the analysis of wideband signals (*9*). We chose this approach to sufficiently capture the multiple frequency bands associated with the SWD as shown in the spectrogram in Fig. 5D. In short, the GP captures the phase of the largest fluctuation on the recording electrode at any moment in time without distortions due to large low-frequency intrusions or smaller high-frequency inclusions (Fig. 5E). We applied this method to the LFP signal pretreated with a wide bandpass (5 to 40 Hz; eighth-order zero-phase Butterworth filter).

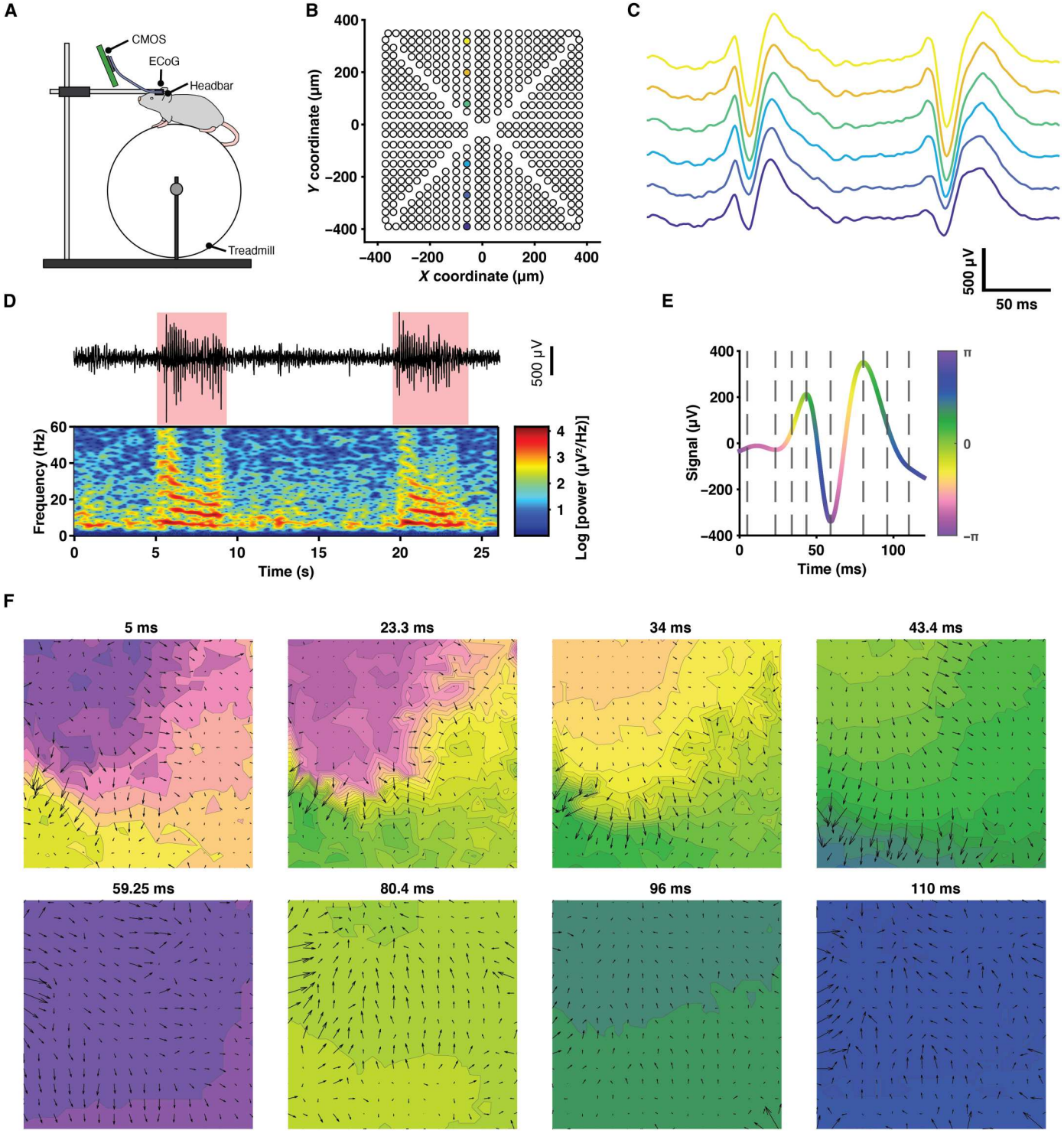

Fig. 5. In vivo recording in an awake and moving mouse. (**A**) Schematic of a head-fixed epileptic mouse on a treadmill. A 2-mm-diameter craniotomy exposes the cortex upon which a 504-channel ECoG array spanning 0.76 mm by 0.76 mm is laid. (**B** and **C**) ECoG electrode layout and representative traces showing SWDs during a seizure, color-coded to match their respective positions. (**D**) Top: Representative trace of a single channel with two seizures highlighted in red. Bottom: Corresponding spectrogram showing the decrease in the frequency band across the duration of the seizure, characteristic of absence epilepsy. (**E**) Representative trace color-coded according to the instantaneous phase of the signal. (**F**) Heatmap of the instantaneous phase across the electrode arrays during a single SWD. Each frame corresponds to a dotted line in Fig. 3E.

Figure 5F shows snapshots of the spatial variation of the phase throughout the time course of a single SWD. Here, we observed complex traveling wave behavior that constantly shifted in direction and velocity, even across the duration of a single spike SWD. Movie S1 shows a video of the phase evolution across multiple SWDs. Seizure propagation patterns were notably different with time through the seizure, demonstrating that seizure dynamics in absence epilepsy in this model do not have constant propagation trajectories or site of onset. More studies must be conducted to elucidate the origins of this variation. Our high channel density combined with a large area of recording along the cortical surface has allowed an unprecedented level of detail into seizure dynamics at micrometer-level precision.

DISCUSSION

Flex2Chip introduces a facile system design and connectorization method which increases the channel density of ultraconformable, thin-film, flexible devices by 17 times in comparison to state-of-the-art devices. This enables multithousand channel counts on a single ASIC, unlike current approaches, which rely on the modularization of multiple ASICs and circuit boards (*11*, *17*, *19*, *32*). The assembly method is simple, consisting of placing the device on a CMOS-MEA with a thin layer of IPA. As the IPA dries, the microstructures self-assemble in their collapsed configuration. The connectorization does not require specialized equipment as needed for wire bonding, anisotropic conductive film (*15*), or ultrasonic-on-bump bonding (*16*).

Here, the key limitation to pad density is not the interconnection interfacial area but the routing of the traces. Although we demonstrate that we can form interconnections with a pitch of 50 μm with a theoretical density of 400 channels/mm^2, the density for our 2200-channel devices is 272 channels/mm^2 even with 1-μm-wide traces with 1-μm spacing. The input-referred noise level in the action potential range (300 Hz to 10 kHz) is 6.93 ± 3.30 μV_{rms}, comparable to that of monolithic silicon probes such as the Neuropixels 2.0 (8.2 μV_{rms}) (*33*).

The bonding methodology is agnostic to the chip, and rapid progress in their functionality—such as the addition of fast scan cyclic voltammetry, impedance spectroscopy, stimulation artifact suppression units, etc.—can be facilely extended to the polymer device (*34*). Furthermore, it is also agnostic to downstream geometry, as shown here with both acute brain slice and in vivo cortical recordings. The developed technology can be easily used to extend the work on cutting-edge chronic intracortical and organoid recordings with mesh electronics (*35*–*37*). Improvements to miniaturize the CMOS-MEA onto a headstage for freely behaving mice experiments are already on the way.

MATERIALS AND METHODS

Flex2Chip device fabrication

The devices were fabricated using standard microfabrication processes. The fabrication steps are as follows: (i) A 4-inch silicon wafer (P-type silicon, 0.1 to 0.9 ohm/cm; Silicon Valley Microelectronics Inc., CA, USA) was cleaned with O_2 plasma [27.6 standard cubic centimeter per minute (sccm), 50 W, 300 mtorr, 1 min; PE II-A, Technics, CA, USA]. (ii) Alignment marks were patterned on the wafer. First, the wafer was dehydrated at 150°C and primed with hexamethyldisilazane (YES LP-III, Yield Engineering Systems, USA). Second, a 0.7-μm-thick layer of positive photoresist (I Line SPR 955 CM-0.7, Dow, MI, USA) was spin-coated on the wafer (1700 rpm, 30 s) and baked (90°C, 120 s). Third, the alignment marks were exposed (150 mW/cm^2; PAS 5500/60, ASML, Veldhoven, The Netherlands). Fourth, after exposure, the resist was baked (90 s), developed with MF-26A (60 s, Dow, MI, USA), rinsed with water, and hard-baked (110°C, 60 s). Fifth, the alignment marks were etched 120-nm deep into SiO_2 (100 sccm CF_4, 2 sccm O_2, 500 W, 250 mtorr, 40 s; P5000, Applied Materials, CA, USA). Last, the photoresist was stripped using a microwave plasma system (LoLamp, 45 s; Aura Asher, Gasonics, CA, USA). (iii) A 250-nm-thick Ni sacrificial layer was deposited with electron beam evaporation (2.5 Å/s, 6×10^{-7} torr; ES26C, Innotec, MI, USA). (iv) A 1-μm-thick layer of polyimide (PI2610, Dupont, DE, USA) forming the substrate base was spin-coated (3000 rpm, 60 s), soft-baked (90°C, 3 min), and finally hard-baked in an inert N_2 atmosphere (325°C, 30 min, 2°C/min ramp; Blue-M, PA, USA). (v) A metallic layer, which forms the electrodes, interconnects, and bonding pads, was then deposited. First, a 200-nm-thick liftoff layer (Microposit LOL 2000, Dow, MI, USA) was spin-coated (3000 rpm, 60 s) and baked (200°C, 7 min). Second, positive photoresist was patterned as described above. Third, the photoresist was descummed with O_2 plasma (27.6 sccm, 50 W, 300 mtorr, 2.5 min; PE II-A, Technics, CA, USA). Fourth, a 10-nm-thick Cr and 100-nm-thick Pt layer were deposited with electron beam evaporation (1 Å/s, 6×10^{-7} torr; ES26C, Innotec, MI, USA). Last, the photoresist was lifted off overnight (Microposit Remover 1165, Dow, MI, USA). (vi) A 1-μm-thick layer of polyimide, which formed the insulating layer, was spin-coated as described above. (vii) A negative mask, which defined the shape of the device and the exposure of the electrode pads, was deposited. First, positive photoresist was patterned and descummed as described above. Second, a 50-nm-thick Ni layer was deposited with electron beam evaporation (1 Å/s, 6×10^{-7} torr; ES26C, Innotec, MI, USA). Third, the photoresist was lifted off as described above. Fourth, the unprotected polyimide was then etched with O_2 plasma (60 sccm O_2, 400 W, 200 mtorr, 100 s; P5000, Applied Materials, CA, USA). (viii) Last, the Si wafer was transferred to an Ni etchant solution (40% $FeCl_3$:39% HCl:H_2O = 1:1:20) to remove the sacrificial Ni layer and negative mask and to release the device from the Si wafer.

CMOS-MEA modifications

The CMOS-MEA (MaxWell Biosystems, Zurich, Switzerland) has 26,400 pixels, 1024 of which can be arbitrarily chosen to record from simultaneously at 20 kHz (*23*). The bare die was wire-bonded to custom printed circuit boards (PCBs) (3100 Plus, ESEC, Cham, Switzerland). The wirebonds were then encapsulated with epoxy (353ND-T, Epoxy Technology, MA, USA). Here, the pixels were recessed by a 1.2-μm-thick layer of SiO_2 and SiN_x. To elevate the pixel, Au was electrochemically deposited (60 s, 1.5 V, NB Semiplate AU 100 AS, Microchemicals, Ulm, Germany) using a Pt counter electrode.

Flex2Chip device assembly

For the device assembly, it is critical to minimize the number of particles to maximize the connectivity yield. The assembly of the device onto the CMOS-MEA is as follows. (i) The CMOS-MEA was transferred to a bath of submicrometer-filtered IPA (Millipore Sigma,

MA, USA, PX1838), cleaned by ultrasonication for 30 s, and blown dry. (ii) A thin layer of IPA was applied using a pipette on the surface of the CMOS-MEA to form a stable liquid film, and the device was then placed on top with a pair of paintbrushes. The capillary forces from the liquid bridge acts to pull the bulk device flat, preventing the buckling of the device during transfer and manipulation. Furthermore, the liquid film also reduces the friction coefficient between the CMOS-MEA and device when sheared, enabling sliding without damaging the device. Paintbrushes were chosen as opposed to forceps as their softness prevents scratching of the device during manipulation and provides a mechanical spring–like buffer between the hand and device. As a result, once the device is placed on top of the CMOS-MEA, the paintbrushes can be used to gently drag the device into approximate alignment on top of the active region of the chip. Subsequently, as the IPA dries, the pads are then self-assembled onto the pixels. (iii) The device was then sterilized in 70% ethanol solution for 1 hour and exposed to ultraviolet for 3 min.

Electrical characterization

Impedance and *I-V* curve measurements were conducted on a CMOS-MEA phantom using a potentiostat (SP-200, BioLogic, Seyssinet-Pariset, France). The distal end of the device was shorted to a gallium droplet to ensure ohmic contact to probe the Flex2Chip interface at the proximal end. Connectivity, noise, and signal attenuation measurements were conducted on the CMOS-MEA, as described by previous work (*23*). The distal end of the device was immersed in a PBS bath (Thermo Fisher Scientific, MA, USA, 10010-023) along with a Pt counter electrode. For connectivity and signal attenuation measurements, the gain of the amplifiers was set to 24, and a 1-kHz 5-mV sine wave was injected at the counter electrode. Pixels connected to Flex2Chip microstructures would then record the sinusoidal waveform, and the corresponding pad could then be mapped. The attenuation was calculated to be the ratio between the measured and injected signal. Pt black coating (100 mM hexachloroplatinic acid, Millipore Sigma, MA, USA, 206083) was electrochemically deposited (0.5 V, 30 s) under mechanical agitation to lower the electrode-electrolyte impedance.

Device encapsulation

The devices could be encapsulated by applying a liquid silicone elastomer (KwikSil, World Precision Instruments Inc., FL, USA) over the Flex2Chip interface. The silicone elastomer was cured after 10 min, after which the connectivity and mechanically robustness were subsequently assessed.

The tensile forces were measured by mounting one end of the device on a z stage and the other on a weighing balance (PM4000, Mettler Toledo, OH, USA). At the weighing balance, glass slides were attached to the device as miniature weights. The device was then lifted stepwise by the z stage, which gradually lifts the glass slides off the weighing balance. The tensile force experienced by the device was calculated from the decrease in weight at the balance as the glass slides are increasingly supported by the flexible device. At fixed intervals, a current (20 μA) was applied for 5 s, and the average voltage was used to measure the resistance of the interconnect. The measurements were conducted on a CMOS-MEA phantom to probe the interface with a potentiostat (SP-200, BioLogic, Seyssinet-Pariset, France).

Brain slice preparation

All use of mice and experimental protocols were approved by the Basel Stadt veterinary office according to Swiss federal laws on animal welfare. Wild-type mice (male, postnatal day 14, C57BL/6JRj, Janvier Labs) were decapitated under isoflurane anesthesia, and the brains were removed and immersed into ice-cold carbogen-bubbled (95% O_2 + 5% CO_2) artificial cerebrospinal fluid (ACSF) solution containing 125 mM NaCl, 2.5 mM KCl, 25 mM glucose, 1.25 mM NaH_2PO_4, 25 mM $NaHCO_3$, 2 mM $CaCl_2$, and 1 mM $MgCl_2$. The cerebellum was dissected and glued on the cutting stage of a vibratome (VT1200S, Leica, Wetzlar, Germany). Sagittal cerebellar slices with a thickness of 380 μm were obtained. Slices were then maintained in ACSF at room temperature until use.

A 6-mm-diameter stainless steel ring was bonded to a 720-channel device using cyanoacrylate adhesive (Pattex, Henkel, Aachen, Germany), where the exposed platinum electrodes were facing away from the ring. The construct was placed on the acute slice and held in place with the stainless steel ring. The tissue was continuously perfused with carbogen-bubbled ACSF at 33° to 36°C to maintain cell viability.

In vivo preparation

Mice with the heterozygous loss of function mutation in *Scn8a* [male, 12 weeks old, C3HeB/FeJ-Scn8amed/J, the Jackson Laboratory, stock no. 003798 (*38*)], referred to here as *Scn8a*$^{+/-}$, were the vertebrate animal subjects used for in vivo measurements. All procedures performed on the mice were approved by Stanford University's Administrative Panel on Laboratory Animal Care (protocol no. 12363). The animal care and use programs at Stanford University meet the requirements of all federal and state regulations governing the humane care and use of laboratory animals, including the United States Department of Agriculture Animal Welfare Act and the Public Health Service Policy on Humane Care and Use of Laboratory Animals. The laboratory animal care program at Stanford is accredited by the Association for the Assessment and Accreditation of Laboratory Animal Care. All mice were maintained on a reverse 12-hour dark/12-hour light cycle (temperature: 20° to 25°C; humidity: 50 to 65%) in the Stanford University's Veterinary Service Center and fed with food and water ad libitum as appropriate. All experiments occurred during their active cycle.

Surgery

Anesthesia was induced with isoflurane (4%; maintained at 1.5%) followed by injection of carprofen (2 mg/kg). Fiducial marks were marked on the skull at the following coordinates from bregma: anteroposterior, −0.85 mm; mediolateral, 2.5 mm. A self-tapping bone screw (Fine Science Tools, CA, USA, 19010-10) was set in the skull over the cerebellum. A stainless steel headbar was cemented onto the skull using dental cement (C&B Metabond, Parkell, NY, USA). After headbar implantation, mice were habituated to run on a treadmill for 7 days. In a second surgical procedure, a 2-mm-diameter craniotomy was then made over the fiducial mark and covered with KwikCast (World Precision Instruments, FL, USA). The mouse then recovered overnight before the recording session.

Electrophysiological recording

Once mounted on the treadmill, the KwikCast above the craniotomy was removed, and the well was filled with saline (0.9% NaCl).

The ECoG device was lain on the surface of the cortex, and the saline was wicked away to allow sufficient contact between the device and cortex. KwikCast was then reapplied. The CMOS-MEA counter electrode operates at a reference voltage of 1.65 V. Consequently, the animal was isolated from the ground by connecting the reference of the chip to a skull screw. Recording then lasted for 40 min.

Spike sorting

Data analysis was performed using custom software written in Python 3.9.0 and MATLAB 2019b (MathWorks, MA, USA). Automatic spike sorting was performed using Kilosort 3 (https://github.com/MouseLand/Kilosort) (*33*, *39*). Subsequently, using the ecephys spike sorting pipeline (https://github.com/AllenInstitute/ecephys_spike_sorting), double counted spikes were removed from each cluster (within ±0.16 ms), and the ISI violations within the refractory period (± 1.5 ms) were calculated. Units were only classified as good if the number of spikes was greater than 100, the ISI violations were less than 0.1, and if Kilosort 3 originally labeled the spike as "good." Last, clusters were inspected and curated in Phy (https://github.com/cortex-lab/phy).

Supplementary Materials

This PDF file includes:
Figs. S1 to S6
Legend for movie S1

Other Supplementary Material for this manuscript includes the following:
Movie S1

View/request a protocol for this paper from *Bio-protocol*.

REFERENCES AND NOTES

1. J. F. Hipp, D. J. Hawellek, M. Corbetta, M. Siegel, A. K. Engel, Large-scale cortical correlation structure of spontaneous oscillatory activity. *Nat. Neurosci.* **15**, 884–890 (2012).
2. L. Huber, E. S. Finn, D. A. Handwerker, M. Bönstrup, D. R. Glen, S. Kashyap, D. Ivanov, N. Petridou, S. Marrett, J. Goense, B. A. Poser, P. A. Bandettini, Sub-millimeter fMRI reveals multiple topographical digit representations that form action maps in human motor cortex. *Neuroimage* **208**, 116463 (2020).
3. Y. Yang, M. R. DeWeese, G. H. Otazu, A. M. Zador, Millisecond-scale differences in neural activity in auditory cortex can drive decisions. *Nat. Neurosci.* **11**, 1262–1263 (2008).
4. D. A. Moses, S. L. Metzger, J. R. Liu, G. K. Anumanchipalli, J. G. Makin, P. F. Sun, J. Chartier, M. E. Dougherty, P. M. Liu, G. M. Abrams, A. Tu-Chan, K. Ganguly, E. F. Chang, Neuroprosthesis for decoding speech in a paralyzed person with anarthria. *N. Engl. J. Med.* **385**, 217–227 (2021).
5. G. K. Anumanchipalli, J. Chartier, E. F. Chang, Speech synthesis from neural decoding of spoken sentences. *Nature* **568**, 493–498 (2019).
6. G. Hotson, D. P. McMullen, M. S. Fifer, M. S. Johannes, K. D. Katyal, M. P. Para, R. Armiger, W. S. Anderson, N. V. Thakor, B. A. Wester, N. E. Crone, Individual finger control of a modular prosthetic limb using high-density electrocorticography in a human subject. *J. Neural Eng.* **13**, 026017 (2016).
7. E. Boran, G. Ramantani, N. Krayenbühl, M. Schreiber, K. König, T. Fedele, J. Sarnthein, High-density ECoG improves the detection of high frequency oscillations that predict seizure outcome. *Clin. Neurophysiol.* **130**, 1882–1888 (2019).
8. L. Muller, G. Piantoni, D. Koller, S. S. Cash, E. Halgren, T. J. Sejnowski, Rotating waves during human sleep spindles organize global patterns of activity that repeat precisely through the night. *eLife* **5**, e17267 (2016).
9. Z. W. Davis, L. Muller, J. Martinez-Trujillo, T. Sejnowski, J. H. Reynolds, Spontaneous traveling cortical waves gate perception in behaving primates. *Nature* **587**, 432–436 (2020).
10. D. Khodagholy, J. N. Gelinas, T. Thesen, W. Doyle, O. Devinsky, G. G. Malliaras, G. Buzsáki, NeuroGrid: Recording action potentials from the surface of the brain. *Nat. Neurosci.* **18**, 310–315 (2015).
11. Y. Tchoe, A. M. Bourhis, D. R. Cleary, B. Stedelin, J. Lee, K. J. Tonsfeldt, E. C. Brown, D. A. Siler, A. C. Paulk, J. C. Yang, H. Oh, Y. G. Ro, K. Lee, S. M. Russman, M. Ganji, I. Galton, S. Ben-Haim, A. M. Raslan, S. A. Dayeh, Human brain mapping with multithousand-channel PtNRGrids resolves spatiotemporal dynamics. *Sci. Transl. Med.* **14**, eabj1441 (2022).
12. C.-H. Chiang, S. M. Won, A. L. Orsborn, K. J. Yu, M. Trumpis, B. Bent, C. Wang, Y. Xue, S. Min, V. Woods, C. Yu, B. H. Kim, S. B. Kim, R. Huq, J. Li, K. J. Seo, F. Vitale, A. Richardson, H. Fang, Y. Huang, K. Shepard, B. Pesaran, J. A. Rogers, J. Viventi, Development of a neural interface for high-definition, long-term recording in rodents and nonhuman primates. *Sci. Transl. Med.* **12**, eaay4682 (2020).
13. K. Scholten, C. E. Larson, H. Xu, D. Song, E. Meng, A 512-channel multi-layer polymer-based neural probe array. *J. Microelectromechanical Syst.* **29**, 1054–1058 (2020).
14. S. Guan, J. Wang, X. Gu, Y. Zhao, R. Hou, H. Fan, L. Zou, L. Gao, M. Du, C. Li, Y. Fang, Elastocapillary self-assembled neurotassels for stable neural activity recordings. *Sci. Adv.* **5**, eaav2842 (2019).
15. P. Ledochowitsch, R. J. Félus, R. R. Gibboni, A. Miyakawa, S. Bao, M. M. Maharbiz, Fabrication and testing of a large area, high density, parylene MEMS μECoG array, in *2011 IEEE 24th International Conference on Micro Electro Mechanical Systems* (2011), pp. 1031–1034.
16. J. J. Yoo, E. Meng, Bonding methods for chip integration with parylene devices. *J. Micromechanics Microengineering* **31**, 045011 (2021).
17. Z. Zhao, H. Zhu, X. Li, L. Sun, F. He, J. E. Chung, D. F. Liu, L. Frank, L. Luan, C. Xie, Ultraflexible electrode arrays for months-long high-density electrophysiological mapping of thousands of neurons in rodents. *Nat. Biomed. Eng.* **7**, 520–532 (2023).
18. J. E. Chung, H. R. Joo, J. L. Fan, D. F. Liu, A. H. Barnett, S. Chen, C. Geaghan-Breiner, M. P. Karlsson, M. Karlsson, K. Y. Lee, H. Liang, J. F. Magland, J. A. Pebbles, A. C. Tooker, L. F. Greengard, V. M. Tolosa, L. M. Frank, High-density, long-lasting, and multi-region electrophysiological recordings using polymer electrode arrays. *Neuron* **101**, 21–31.e5 (2019).
19. E. Musk; Neuralink, An integrated brain-machine interface platform with thousands of channels. *J. Med. Internet Res.* **21**, e16194 (2019).
20. J. Viventi, D.-H. Kim, L. Vigeland, E. S. Frechette, J. A. Blanco, Y.-S. Kim, A. E. Avrin, V. R. Tiruvadi, S.-W. Hwang, A. C. Vanleer, D. F. Wulsin, K. Davis, C. E. Gelber, L. Palmer, J. Van der Spiegel, J. Wu, J. Xiao, Y. Huang, D. Contreras, J. A. Rogers, B. Litt, Flexible, foldable, actively multiplexed, high-density electrode array for mapping brain activity in vivo. *Nat. Neurosci.* **14**, 1599–1605 (2011).
21. J.-H. Seo, T. Ling, S. Gong, W. Zhou, A. L. Ma, L. J. Guo, Z. Ma, Fast flexible transistors with a nanotrench structure. *Sci. Rep.* **6**, 24771 (2016).
22. K. Sahasrabuddhe, A. A. Khan, A. P. Singh, T. M. Stern, Y. Ng, A. Tadić, P. Orel, C. LaReau, D. Pouzzner, K. Nishimura, K. M. Boergens, S. Shivakumar, M. S. Hopper, B. Kerr, M.-E. S. Hanna, R. J. Edgington, I. McNamara, D. Fell, P. Gao, A. Babaie-Fishani, S. Veijalainen, A. V. Klekachev, A. M. Stuckey, B. Luyssaert, T. D. Y. Kozai, C. Xie, V. Gilja, B. Dierickx, Y. Kong, M. Straka, H. S. Sohal, M. R. Angle, The Argo: A high channel count recording system for neural recording in vivo. *J. Neural Eng.* **18**, 015002 (2021).
23. M. Ballini, J. Müller, P. Livi, Y. Chen, U. Frey, A. Stettler, A. Shadmani, V. Viswam, I. L. Jones, D. Jäckel, M. Radivojevic, M. K. Lewandowska, W. Gong, M. Fiscella, D. J. Bakkum, F. Heer, A. Hierlemann, A 1024-channel CMOS microelectrode array with 26,400 electrodes for recording and stimulation of electrogenic cells in vitro. *IEEE J. Solid-State Circuits.* **49**, 2705–2719 (2014).
24. B. Miccoli, C. M. Lopez, E. Goikoetxea, J. Putzeys, M. Sekeri, O. Krylychkina, S.-W. Chang, A. Firrincieli, A. Andrei, V. Reumers, D. Braeken, High-density electrical recording and impedance imaging with a multi-modal CMOS multi-electrode array chip. *Front. Neurosci.* **13**, 641 (2019).
25. A. Obaid, M.-E. Hanna, Y.-W. Wu, M. Kollo, R. Racz, M. R. Angle, J. Müller, N. Brackbill, W. Wray, F. Franke, E. J. Chichilnisky, A. Hierlemann, J. B. Ding, A. T. Schaefer, N. A. Melosh, Massively parallel microwire arrays integrated with CMOS chips for neural recording. *Sci. Adv.* **6**, eaay2789 (2020).
26. M. Kollo, R. R. Racz, M.-E. S. Hanna, A. M. Obaid, M. R. Angle, W. Wray, Y. Kong, A. Hierlemann, J. Müller, N. A. Melosh, A. T. Schaefer, CHIME: CMOS-hosted in vivo microelectrodes for massively scalable neuronal recordings. *Neuroscience* **14**, 834 (2020).
27. Y. Qiang, W. Gu, Z. Liu, S. Liang, J. H. Ryu, K. J. Seo, W. Liu, H. Fang, Crosstalk in polymer microelectrode arrays. *Nano Res.* **14**, 3240–3247 (2021).
28. J. Mordel, D. Karnas, P. Pévet, P. Isope, E. Challet, H. Meissl, The output signal of purkinje cells of the cerebellum and circadian rhythmicity. *PLOS ONE* **8**, e58457 (2013).
29. D. J. Bakkum, M. E. J. Obien, M. Radivojevic, D. Jäckel, U. Frey, H. Takahashi, A. Hierlemann, The axon initial segment is the dominant contributor to the neuron's extracellular electrical potential landscape. *Adv. Biosyst.* **3**, 1800308 (2019).

30. C. D. Makinson, B. S. Tanaka, J. M. Sorokin, J. C. Wong, C. A. Christian, A. L. Goldin, A. Escayg, J. R. Huguenard, Regulation of thalamic and cortical network synchrony by Scn8a. *Neuron* **93**, 1165–1179.e6 (2017).
31. D. Gabor, Theory of communication. Part 1: The analysis of information. *J. Inst. Electr. Eng.* **3**, 429–441 (1946).
32. S.-Y. Park, K. Na, M. Vöröslakos, H. Song, N. Slager, S. Oh, J. Seymour, G. Buzsáki, E. Yoon, A miniaturized 256-channel neural recording interface with area-efficient hybrid integration of flexible probes and CMOS integrated circuits. *IEEE Trans. Biomed. Eng.* **69**, 334–346 (2022).
33. N. A. Steinmetz, C. Aydin, A. Lebedeva, M. Okun, M. Pachitariu, M. Bauza, M. Beau, J. Bhagat, C. Böhm, M. Broux, S. Chen, J. Colonell, R. J. Gardner, B. Karsh, F. Kloosterman, D. Kostadinov, C. Mora-Lopez, J. O'Callaghan, J. Park, J. Putzeys, B. Sauerbrei, R. J. J. van Daal, A. Z. Vollan, S. Wang, M. Welkenhuysen, Z. Ye, J. T. Dudman, B. Dutta, A. W. Hantman, K. D. Harris, A. K. Lee, E. I. Moser, J. O'Keefe, A. Renart, K. Svoboda, M. Häusser, S. Haesler, M. Carandini, T. D. Harris, Neuropixels 2.0: A miniaturized high-density probe for stable, long-term brain recordings. *Science* **372**, eabf4588 (2021).
34. J. Dragas, V. Viswam, A. Shadmani, Y. Chen, R. Bounik, A. Stettler, M. Radivojevic, S. Geissler, M. Obien, J. Müller, A. Hierlemann, A multi-functional microelectrode array featuring 59760 electrodes, 2048 electrophysiology channels, stimulation, impedance measurement and neurotransmitter detection channels. *IEEE J. Solid-State Circuits* **52**, 1576–1590 (2017).
35. X. Yang, T. Zhou, T. J. Zwang, G. Hong, Y. Zhao, R. D. Viveros, T.-M. Fu, T. Gao, C. M. Lieber, Bioinspired neuron-like electronics. *Nat. Mater.* **18**, 510–517 (2019).
36. S. Zhao, X. Tang, S. Partarrieu, S. Guo, R. Liu, J. Lee, Z. Lin, J. Liu, Tracking neural activity from the same cells during the entire adult life of mice. *Nat. Neurosci.* **26**, 696–710 (2021).
37. P. Le Floch, Q. Li, Z. Lin, S. Zhao, R. Liu, K. Tasnim, H. Jiang, J. Liu, Stretchable mesh nanoelectronics for 3D single-cell chronic electrophysiology from developing brain organoids. *Adv. Mater.* **34**, 2106829 (2022).
38. D. C. Kohrman, J. B. Harris, M. H. Meisler, Mutation detection in the *med* and *med*^{J} Alleles of the sodium channel *Scn8a*: Unusual splicing due to a minor class AT-AC intron*. *J. Biol. Chem.* **271**, 17576–17581 (1996).
39. M. Pachitariu, N. A. Steinmetz, S. N. Kadir, M. Carandini, K. D. Harris, Fast and accurate spike sorting of high-channel count probes with KiloSort, in *Advances in Neural Information Processing Systems* (Curran Associates Inc., 2016), vol. 29; https://proceedings.neurips.cc/paper/2016/hash/1145a30ff80745b56fb0cecf65305017-Abstract.html.

Acknowledgments
Funding: Research at Stanford was supported by the Wu Tsai Institute Big Ideas program. E.T.Z. was supported by the Bio-X Stanford Interdisciplinary Fellowship and Croucher Scholarship. Part of this work was performed at the Stanford Nanofabrication Facility (SNF), supported by the National Science Foundation under award ECCS-2026822. The CMOS-MEA work was supported by the European Union under the ERC advanced grant "neuroXscales" (contract 694829). **Author contributions:** E.T.Z. and N.A.M. conceived the experiments. E.T.Z. and P.W. fabricated the devices. E.T.Z. and A.P. developed the assembly process. E.T.Z., N.M.H., H.U., and A.Z. characterized the devices. H.U., S.R., and E.T.Z. prepared the CMOS-MEAs. J.M.H. and E.T.Z. performed experiments in rodents and analyzed the data. J.B. and E.T.Z. performed experiments on cerebellar slices and analyzed the data. N.A.M., A.H., and J.R.H. supervised the work. E.T.Z. and N.A.M. wrote the manuscript with contribution from all the authors. Cartoons in Fig. 1A were created with BioRender.com. **Competing interests:** N.A.M. is a cofounder in Paradromics Inc., a company developing scalable electrophysiology. S.R. is now employed at MaxWell Biosystems AG, a company that fabricates and commercializes high-density microelectrode arrays. The authors declare that they have no other competing interests. **Data and materials availability:** All data needed to evaluate the conclusions in the paper are present in the paper and/or the Supplementary Materials.

Submitted 22 November 2022
Accepted 3 May 2023
Published 7 June 2023
10.1126/sciadv.adf9524